Article

Oxidation-resistant all-perovskite tandem solar cells in substrate configuration

Yurui Wang[1,5], Renxing Lin[1,5], Xiaoyu Wang [2,5], Chenshuaiyu Liu[1], Yameen Ahmed [3], Zilong Huang[1], Zhibin Zhang [4], Hongjiang Li[1], Mei Zhang[1], Yuan Gao[1], Haowen Luo[1], Pu Wu[1], Han Gao[1], Xuntian Zheng[1], Manya Li[1], Zhou Liu[1], Wenchi Kong[1], Ludong Li [1], Kaihui Liu [4], Makhsud I. Saidaminov [3], Lijun Zhang [2] & Hairen Tan [1] ✉

The commonly-used superstrate configuration (depositing front subcell first and then depositing back subcell) in all-perovskite tandem solar cells is disadvantageous for long-term stability due to oxidizable narrow-bandgap perovskite assembled last and easily exposable to air. Here we reverse the processing order and demonstrate all-perovskite tandems in a substrate configuration (depositing back subcell first and then depositing front subcell) to bury oxidizable narrow-bandgap perovskite deep in the device stack. By using guanidinium tetrafluoroborate additive in wide-bandgap perovskite subcell, we achieve an efficiency of 25.3% for the substrate-configured all-perovskite tandem cells. The unencapsulated devices exhibit no performance degradation after storage in dry air for 1000 hours. The substrate configuration also widens the choice of flexible substrates: we achieve 24.1% and 20.3% efficient flexible all-perovskite tandem solar cells on copper-coated polyethylene naphthalene and copper metal foil, respectively. Substrate configuration offers a promising route to unleash the commercial potential of all-perovskite tandem solar cells.

Monolithic all-perovskite tandem solar cells include a front subcell with ~1.8 eV wide-bandgap (WBG) perovskite and a back subcell with ~1.2 eV narrow-bandgap (NBG) perovskite[1–3]. All-perovskite tandem solar cells have achieved a record certified efficiency of 26.4%, exceeding the single-junction perovskite solar cells (PSCs)[1,2,4,5]. But oxygen-related instability remains a key challenge for their commercialization[6–8]. Encapsulation can prevent oxygen-induced degradation in the active layers or electrodes; however, oxidation can still occur during the module processing and/or air leakage during operation. For flexible all-perovskite tandem solar cells, polymer substrates with high transparency are typically needed, limiting the choice of substrates and increasing the cost of flexible devices[9]. Therefore,

new device structures that can allow higher resistance to oxygen and lower material cost for flexible devices are needed.

Reported all-perovskite tandems[2,3,10–13], either rigid or flexible, typically use a "superstrate configuration" structure (Fig. 1a)[14,15]. In this structure, WBG front subcell is deposited first on a rigid or flexible transparent conductive substrate (e.g., glass/ITO or PEN/ITO), followed by the tunneling recombination junction (TRJ), NBG back subcell, and metal back electrode. In this configuration, sunlight first passes through the front transparent substrate, and then is absorbed in the front subcell and the back subcell in sequence. This structure has been widely implemented and is compatible with low-cost solution processing.

[1]National Laboratory of Solid State Microstructures, College of Engineering and Applied Sciences, Frontiers Science Center for Critical Earth Material Cycling, Nanjing University, Nanjing 210023, China. [2]State Key Laboratory of Superhard Materials, Key Laboratory of Automobile Materials of MOE, College of Materials Science and Engineering, Jilin University, Changchun, China. [3]Department of Chemistry, University of Victoria, Victoria, BC, Canada. [4]State Key Laboratory for Mesoscopic Physics, Frontiers Science Center for Nano-optoelectronics, School of Physics, Peking University, Beijing, China. [5]These authors contributed equally: Yurui Wang, Renxing Lin, Xiaoyu Wang. ✉e-mail: hairentan@nju.edu.cn
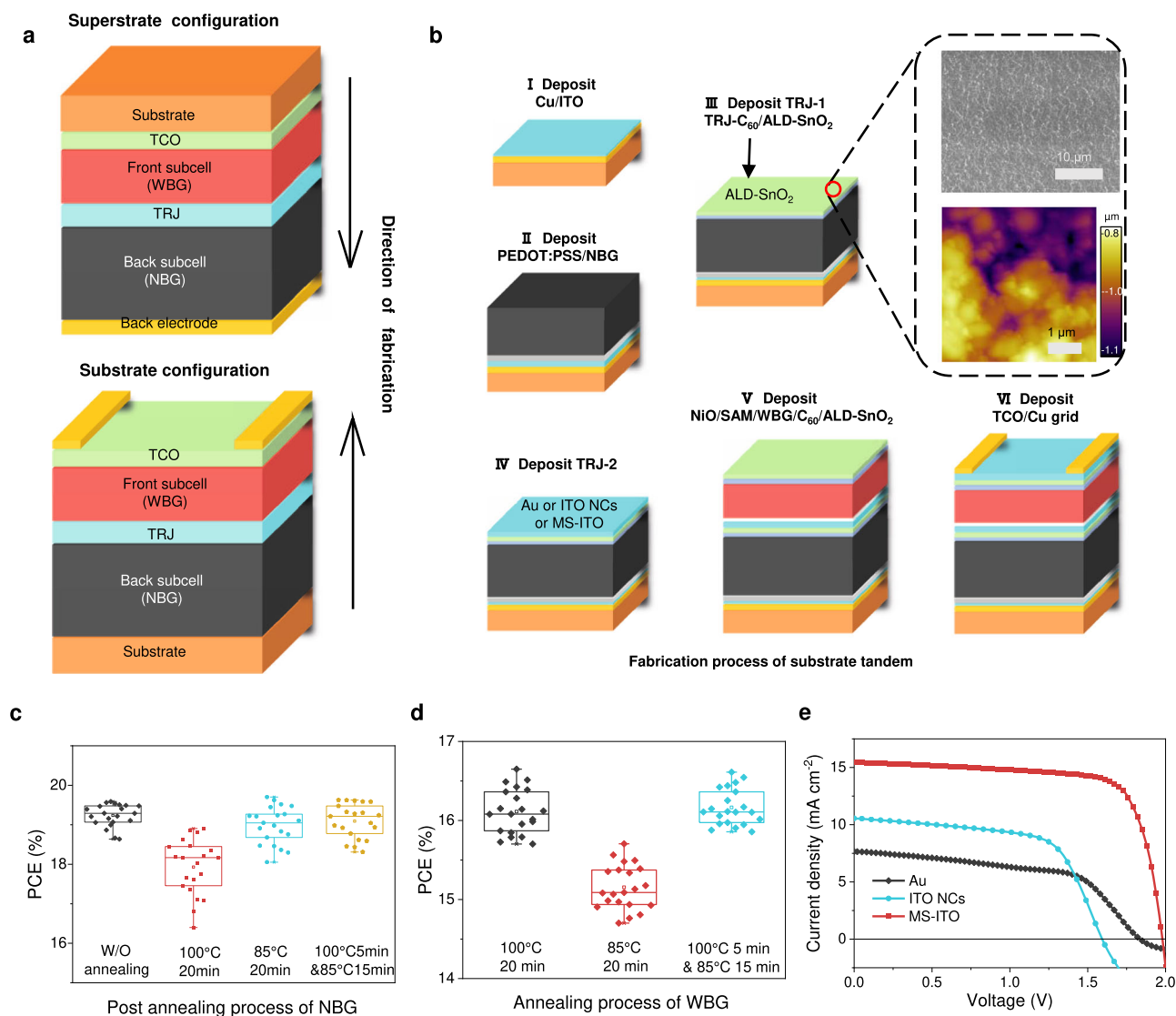
Fig. 1 | Design and fabrication process of all-perovskite tandem solar cells in substrate configuration. a Device structure of superstrate- and substrate-configured all-perovskite tandem solar cells. **b** Fabrication process of all-perovskite tandem solar cells in substrate configuration. **c** Effect of post-annealing conditions on semitransparent narrow-bandgap PSCs. **d** Effect of annealing conditions on semitransparent wide-bandgap PSCs. There are 21 devices for each type in b and c, and the box lines indicate the standard deviation, and the centre represents the mean value. **e** J–V curves of substrate-configurated all-perovskite tandem solar cells with Au or ITO nanocrystals (ITO NCs) or magnetron-sputtered ITO (MS-ITO) as the recombination layer.

However, externally exposed NBG perovskites, made of mixed lead-tin (Pb-Sn), are more sensitive to oxygen than WBG perovskites buried at the bottom, making the superstrate configuration an inherent disadvantage to device stability. Pb-based PSCs have been widely proven to be stable in air for a period of time without degradation of performance[16,17]. But this is not the case for Pb-Sn-based perovskites: Sn^{2+} in NBG perovskite is oxidized to form Sn^{4+} on a minute scale in the presence of oxygen, leading to high trap densities and short diffusion lengths, and thus device degradation[18,19]. The oxidation of Sn^{2+} can be inhibited by comproportionation[2] or reducing additives like tin (II) fluoride (SnF_2)[20–22] or others[23,24]. This strategy improves the quality of the precursor solution and device performance. Coating a thin layer of metal oxide (e.g., SnO_2) made by atomic layer deposition (ALD) on top of Pb-Sn perovskite layer can by some extent prevent the penetration of oxygen into the absorber layer and thus improve the air stability in tandem devices, but this only provides limited protection[24,25]. The oxidation of Sn^{2+} remains a major challenge for the long-term stability of all-perovskite tandem solar cells.

Here we sought to devise all-perovskite tandem solar cells with a substrate-configured device structure (illustrated in Fig. 1a), in which easily oxidizable NBG back subcell is deposited first and is buried at the bottom of the tandem device. In the substrate configuration, TRJ and front subcell offer a self-encapsulation for the NBG perovskite, effectively preventing the penetration of oxygen into the mixed Pb-Sn perovskite absorber layer. In addition, this configuration does not demand the substrate to be transparent, thus widening the choice from transparent substrates (e.g., glass, polyethylene terephthalate (PET)[26], polyethylene naphthalate (PEN)[27] and polyimide (PI)[28]) to opaque and high-temperature tolerant flexible polymers, stainless steel[29] and metal foils[30]. This allows lower cost for lightweight and flexible all-perovskite tandem solar modules[13]. By adopting a substrate configuration, we demonstrated rigid all-perovskite tandem solar cells with a PCE of 25.3%. The unencapsulated devices exhibited impressive tolerance to oxygen and maintained their initial performance when stored in dry air for more than 1000 hours. The encapsulated devices maintained 100% of their initial performance after 600 hours of

operation at maximum power point in ambient conditions. The substrate configuration also enabled the fabrication of efficient flexible all-perovskite tandem solar cells on metal-coated polymer substrates and metal foils.

Results

Fabrication of substrate-configured tandems

The fabrication process of substrate-configured all-perovskite tandem solar cell is illustrated in Fig. 1b. We chose Cu/ITO as the back electrode; this also eased the transfer of devices to metal substrates, as we will show below. In step I, a thin layer of copper (Cu, 80 nm) was deposited on glass by thermal deposition. A layer of ITO (15 nm) was then sputtered on the substrate to prevent any potential reactions between Cu and perovskite. In step II, the back subcell in PEDOT: PSS/NBG perovskite/C_{60} structure was deposited using our previously reported process[2,24]. In step III, SnO_2 layer was deposited by ALD (ALD-SnO_2) to act as part of TRJ and as a solvent barrier layer. Scanning electron microscopy (SEM) and atomic force microscopy (AFM) were used to observe the surface of ALD-SnO_2 layer deposited on top of the back subcell (Fig. 1b inset). Supplementary Fig. 1 shows the SEM and AFM images of ALD-SnO_2 film on Glass/ITO/NiO/WBG perovskite/C_{60}, the structure of WBG subcell used in superstrate-configured all-perovskite tandems[2,24]. Both configurations showed compact and pinhole-free ALD-SnO_2 films, but significantly higher root-mean-square (RMS) roughness on NBG perovskites (87.9 nm) as compared to that on WBG perovskites (17.2 nm). This is because the thick NBG perovskites tend to have larger grains, resulting in a rougher surface; this makes the construction of TRJ challenging[31].

In TRJ, an additional recombination layer (RL) is required to enable efficient charge recombination[32]. In step IV, we deposited three commonly-used RLs on ALD-SnO_2: a thin layer of gold (Au) by thermal evaporation[2], spin-coated ITO nanocrystals (ITO NCs)[25] and magnetron-sputtered ITO (MS-ITO)[10]. All three RLs allowed a good Ohmic contact when the TRJ was deposited on smooth glass substrates, although with a slight difference in the resistance (Supplementary Fig. 2). However, the substrate-configured tandem devices with Au or ITO NCs as the RL showed "S-shaped" J-V curves and hence low FF values (Fig. 1e). This indicates a Schottky contact formed at TRJ, resulting in poor electron-hole recombination[2]. We speculate that neither Au nor ITO NCs can spread evenly on the rough surface of NBG perovskite/C_{60}/ALD-SnO_2, although they can cover the WBG perovskite/C_{60}/ALD-SnO_2 smooth surface well (Supplementary Fig. 3). We thus chose MS-ITO for the RL: an added benefit for this choice is that inorganic oxides offer longer-term stability than metals used in TRJ[25]. The dense ALD-SnO_2 layer prevents the damage caused by sputtering, and using a thin layer MS-ITO down to 20 nm reduced the parasitic absorption (Supplementary Fig. 4).

In step V, the front subcell with a structure of NiO/SAM/WBG perovskite/C_{60}/ALD-SnO_2 was deposited, in which NiO is nickel oxide and SAM is a self-assembled molecule. Solvent penetration and thermal damages are two major issues while building front subcells on the back cells. As shown in Fig. 1c and Supplementary Fig. 5, the PCE of the NBG PSCs decreased to 85% of its initial value after 20 min of post-annealing at 100 °C. The decreased PV performance is mainly ascribed to the volatile nature of methylammonium (MA)[31,33] and an unfavorable thermal-induced reaction at the PEDOT: PSS/perovskite interface[34,35]. Efforts have been devoted to developing MA-free NBG perovskites and thermally stable HTL materials to improve the thermal stability of NBG PSCs[25,36–38]. We found that relatively low post annealing temperature, i.e. 85 °C, minimizes damage to the NBG-PSCs, but this decreased the PCE of WBG cells (Fig. 1d) likely due to hindered crystallization[39]. Therefore, we combined a lower temperature (85 °C, 15 min) annealing with a higher temperature but shorter time annealing processes (100 °C, 5 min) for the WBG perovskite[40,41]. By using this strategy, we

were able to balance the performance of WBG and NBG subcells simultaneously.

Finally, in step VI, we deposited indium zinc oxide (IZO) by magnetron sputtering on top of the device as the transparent electrode. The tandem cells with MS-ITO as the RJ exhibited a PCE of 22.7%, with a V_{oc} of 1.980 V, a J_{sc} of 15.4 mA cm^{-2}, and a low FF of 74.1%. The V_{oc} of tandem devices is the sum of V_{oc} values of the two subcells. The FF of a current-matched tandem device does correlate with the FF of each subcell[42]. Supplementary Fig. 6 shows that semitransparent NBG subcells (glass/Cu/ITO/PEDOT: PSS/NBG-perovskite/C_{60}/SnO_2/ITO/Cu-grid) can reach a PCE of 19.6% with a high FF of 78.7%. We, therefore, anticipate that further improvement of substrate-configured tandem cells should improve the V_{oc} and FF in the semitransparent WBG subcells.

Semitransparent WBG subcells with GuaBF$_4$ additive

We fabricated semitransparent WBG PSCs with a perovskite composition of $FA_{0.8}Cs_{0.2}Pb(I_{0.6}Br_{0.4})_3$ (~1.77 eV) and NiO/SAM as the HTL[43] (Fig. 2a). However, such semitransparent devices showed low performance mainly due to the low FF and V_{oc} values, compared to the opaque p-i-n PSCs in superstrate configuration (Table 1). We hence sought to use guanidine tetrafluoroborate (GuaBF$_4$) into the perovskite precursor solution. The deep-level defects caused by the high ratio of Br incorporated in WBG perovskites profoundly limit the performance of solar cells[44]. Various large organic cations have been introduced into perovskites for the passivation of halogen defects[45]. Pseudo-halogens have also been reported to inhibit halogen migration[46]. Combined with DFT studies (Supplementary note 1), we reveal that guanidinium (Gua$^+$) avoids the unfavorable lattice distortion and is more effective than phenethylammonium (PEA$^+$)[47] and phenylammonium (PA$^+$)[5] in suppressing halogen vacancy defects (Supplementary Figs. 7–8) due to the stronger hydrogen bonding. The Pb-F bond introduced by tetrafluoroborate (BF$_4^-$) leads to an effective passivation for halogen vacancies[48] (Supplementary Fig. 9). Overall, guanidine tetrafluoroborate (GuaBF$_4$) is expected to inhibit the formation of halogen vacancy defects with minimal effect on the perovskite lattice[49]. The optimized concentration of GuaBF$_4$ added in perovskite precursor solution was found to be 1.5% molar ratio relative to Pb^{2+}. The devices with GuaBF$_4$ additive exhibited an obvious improvement in average V_{oc} and FF compared to the control ones (1.20 V versus 1.24 V; 77.9% versus 80.8%, Table 1 and Supplementary Fig. 10), while the average J_{sc} remained the same. As a result, the GuaBF$_4$ devices showed a considerably higher average PCE (16.7%) than the control devices (15.3%). To reduce the primary optical reflection, we attached a commercially available anti-reflection foil[50] on the top of the substrate-configurated devices (Fig. 2a). The champion GuaBF$_4$ device showed a PCE of 17.3% (with V_{oc} = 1.265 V, J_{sc} = 16.7 mA cm^{-2} and FF = 81.9%), which is higher than that of control device (PCE of 15.8% with V_{oc} = 1.214 V, J_{sc} = 16.5 mA cm^{-2} and FF = 78.1%) (Fig. 2b). The J_{sc} value (16.9 mA cm^{-2}) extracted by integrating the external quantum efficiency (EQE) curve is in good agreement with the J−V characterization (Fig. 2c).

We noted that GuaBF$_4$ also improved the performance of WBG PSCs in superstrate configuration (Supplementary Fig. 11). The average V_{oc} increased from 1.217 V to 1.263 V, while the average FF increased from 79.5% to 82.3%. The champion GuaBF$_4$ device in superstrate configuration exhibited a PCE of 19.1% (V_{oc} = 1.274 V, J_{sc} = 17.7 mA cm^{-2} and FF = 84.5%, Fig. 2d), which is substantially higher than control device (PCE of 17.2% with V_{oc} = 1.221 V, J_{sc} = 17.2 mA cm^{-2} and FF = 81.0%).

We then studied the effect of GuaBF$_4$ additive on perovskite films. X-ray photoelectron spectroscopy (XPS) peaks at 288.5 and 687.3 eV corresponding to Gua (C1s)[1] and F1s[51] confirm the presence of GuaBF$_4$ in perovskite films (Supplementary Fig. 12). Meanwhile, the increased binding energy of Pb peaks (Fig. 2e) suggest a chemical interaction between GuaBF$_4$ and the surface of perovskite grains, since GuaBF$_4$ can bind with uncoordinated Pb^{2+} and/or fill the point vacancies[51]. As
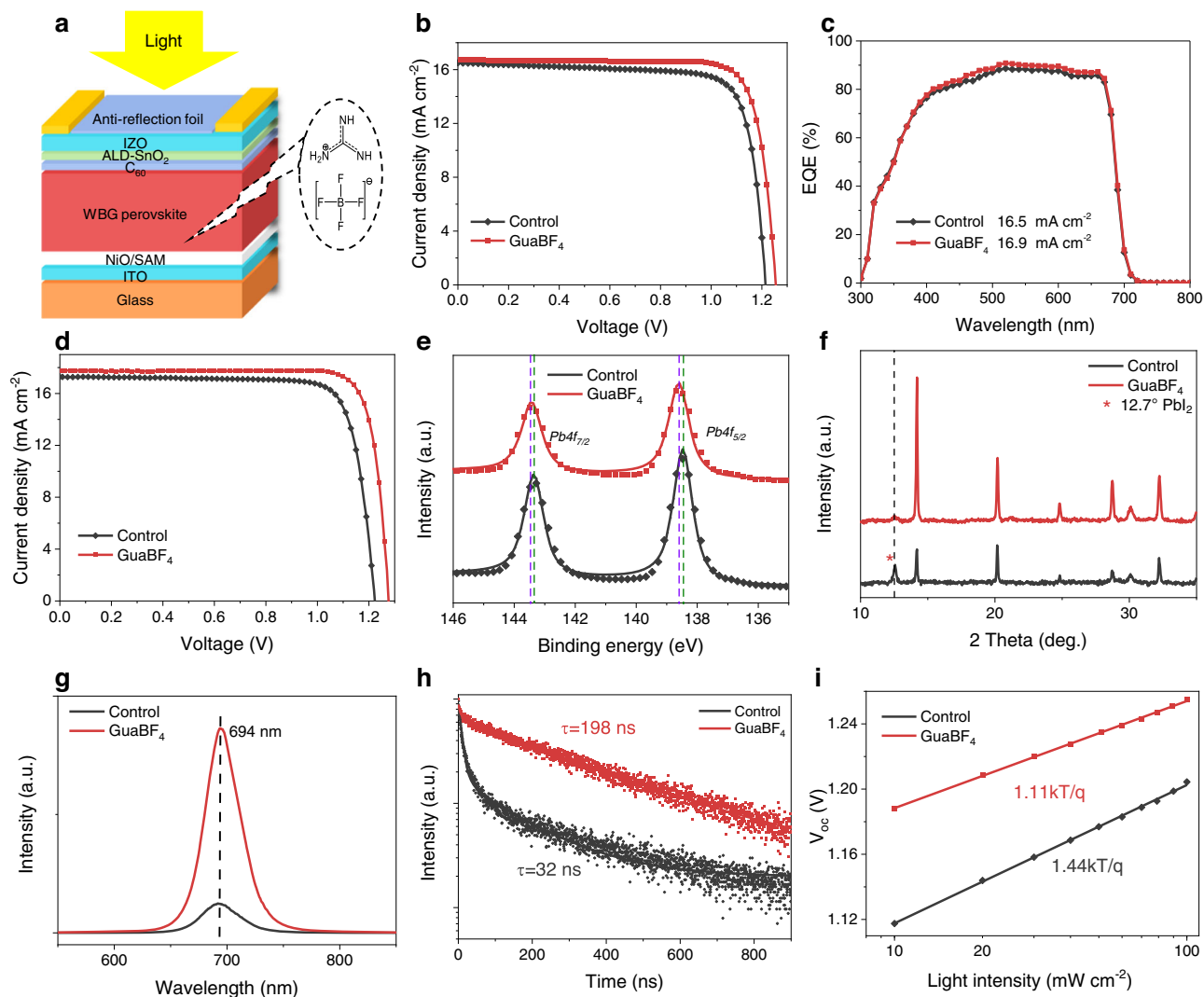
Fig. 2 | Characterization of WBG perovskite films and semitransparent solar cells with GuaBF₄ additive. a Device structure of semitransparent WBG-PSCs. **b** J–V curves of champion control and GuaBF₄ semitransparent WBG-PSCs. **c** EQE spectra of control and GuaBF₄ semitransparent WBG-PSCs. **d** J–V curves of champion control and GuaBF₄ WBG-PSCs in superstrate configuration (device structure shown in Supplementary Fig. 13, The addition of Gua⁺ only (GuaI) shown in Supplementary Fig. 7a). **e** The $Pb\ 4f_{5/2}$ and $Pb\ 4f_{7/2}$ XPS spectra of control and GuaBF₄ perovskite films. **f** The XRD pattern of control and GuaBF₄ perovskite films. **g** Steady-state PL spectra of control and GuaBF₄ perovskite films. **h** TRPL spectra of perovskite films deposited on Glass/ITO. **i** V_{oc} as a function of light intensity plots of the semitransparent WBG-PSCs.

results in reduced binding energy of Pb, which is in contrast to when BF₄⁻ is used. The ionic radii of BF₄⁻ (0.218 nm) and I⁻ (0.220 nm) are nearly the same[52], but BF₄⁻ weakly hybridizes with the atomic orbitals of Pb²⁺, strengthening covalent bond contribution between BF₄⁻ and

Pb²⁺ [53]. The increase in binding energy of Pb²⁺ with GuaBF₄ perovskite film is a concerted effect of Gua⁺ and BF₄⁻, since they, on their own, have opposite effects on the binding energy of Pb²⁺. This is consistent with our DFT calculations.

SEM images (Supplementary Fig. 14) show no obvious change in the grain size of control (319 nm) and GuaBF₄ (356 nm) perovskite films. X-ray diffraction (XRD) shows that GuaBF₄ perovskite film has an enhanced (100) orientation, accompanied by a significantly weakened PbI₂ diffraction peak at 12.7° peak (Fig. 2f). As indicated by the DFT calculations, GuaBF₄ inhibits the formation of vacancy and PbI₂, which helps improve device stability[54]. No obvious shift in XRD peaks was observed, although both Gua⁺ and BF₄⁻ have shown the potential to be introduced into the perovskite lattices[45,48,55,56], indicating that GuaBF₄ mainly exists on the surface and grain boundaries of the perovskite film. Contact angle (CA) tests show that perovskite film with GuaBF₄ (CA = 75°) has a larger contact angle than control sample without GuaBF₄ (CA = 48°), which represents a better surface hydrophobicity (Supplementary Fig. 15). Both control and GuaBF₄ films exhibited photoluminescence (PL) peaks at 694 nm. The latter showed a much stronger PL intensity, indicating reduced non-radiative recombination due to lower trap density in GuaBF₄ sample[57] (Fig. 2g). Time-resolved

Table. 1 | PV performance of single-junction WBG PSCs in substrate and superstrate configurations measured under AM1.5 illumination

Device configuration			V_{oc}(V)	J_{sc}(mA cm⁻²)	FF(%)	PCE(%)
Substrate (semi-transparent, light from IZO)	Average	Control	1.199	16.3	77.9	15.3
		GuaBF₄	1.244	16.5	80.8	16.7
	Champion	Control	1.214	16.5	78.1	15.8
		GuaBF₄	1.265	16.7	81.9	17.3
Superstrate (opaque, light from glass)	Average	Control	1.217	17.1	79.5	16.6
		GuaBF₄	1.263	17.4	82.3	18.4
	Champion	Control	1.221	17.2	81.0	17.2
		GuaBF₄	1.274	17.7	84.5	19.1
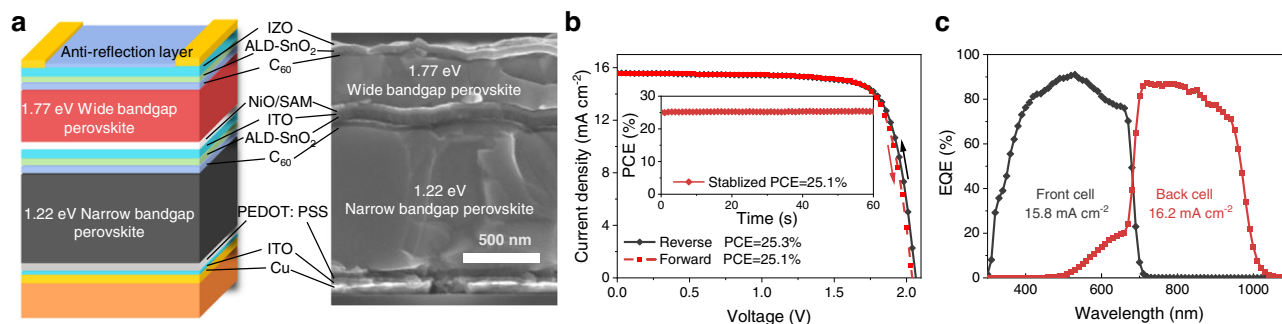
Fig. 3 | Photovoltaic performance of substrate-configured all-perovskite tandem solar cells. a Device structure and corresponding cross-sectional SEM image of substrate-configured tandem solar cells. **b**, **c** J−V curves, EQE spectra, and MPP tracking (inset **b**) of champion GuaBF$_4$ substrate-configured tandem solar cells.

photoluminescence (TRPL) lifetime of the GuaBF$_4$ film (198 ns) was longer than that of the control film (32 ns; Fig. 2h) further indicating suppressed carrier trapping upon the introduction of GuaBF$_4$. This reduced non-radiative recombination leads to the increased V_{oc} in the GuaBF$_4$ devices[58]. Transient photovoltage (TPV) decay showed that the GuaBF$_4$ devices had a longer charge recombination lifetime (τ_{rec}) of 15.4 μs compared to the control one with 2.5 μs (Supplementary Fig. 16). The longer τ_{rec} indicates less recombination in the GuaBF$_4$ devices[59,60], consistent with the results obtained from the PL analysis. Light intensity-dependent V_{oc} analysis shown in Fig. 2i indicates that the GuaBF$_4$ device is closer to unity ideality factor than the control device (1.11 for GuaBF$_4$ and 1.44 for control). Devices with GuaBF$_4$ additive exhibited a lower dark current density than the control devices (Supplementary Fig. 17), consistent with the increase in V_{oc} and FF[20].

Performance of substrate-configured all-perovskite tandems

Motivated by improved V_{oc} and FF in semitransparent WBG PSCs using GuaBF$_4$ additive, we fabricated substrate-configured all-perovskite tandems with a device structure shown in Fig. 3a. The thicknesses of WBG and NBG perovskite layers are ~400 nm and ~1100 nm, respectively. The average PCE of tandem devices increased from 22.6% to 24.1% after adding GuaBF$_4$ in WBG perovskites (Supplementary Fig. 18). Fig 3b presents the J−V curves of the best-performing all-perovskite tandems with GuaBF$_4$, the corresponding PV parameters are summarized in Table 2. The champion GuaBF$_4$ tandem cell exhibited a high PCE of 25.3% under reverse scan, with a V_{oc} of 2.041 V, a J_{sc} of 15.6 mA cm^{-2}, and a FF of 78.9%. The device showed a minor hysteresis between reverse and forward scans (25.3% versus 25.1%). The PCE from J−V sweeps is consistent with the stabilized PCE of 25.1% measured over 60 seconds (Fig. 3b inset). The integrated J_{sc} values from EQE spectra (Fig. 3c) for the WBG (15.8 mA cm^{-2}) and NBG (16.2 mA cm^{-2}) subcells are in good agreement with the J_{sc} determined from J−V measurements.

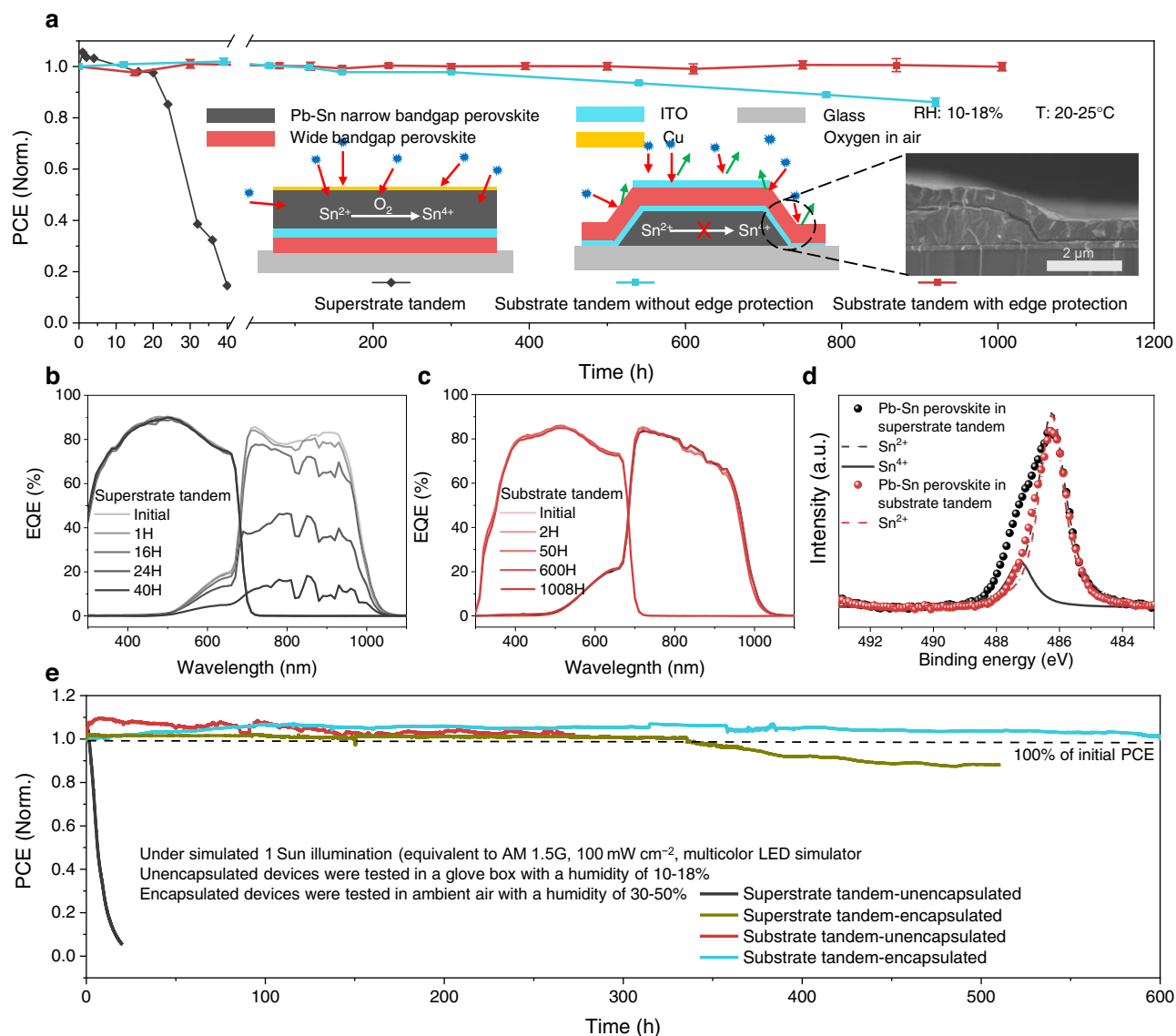## Stability of substrate-configured all-perovskite tandems

We next compared the stability of superstrate- and substrate-configured tandem solar cells (Fig. 4a). The superstrate-configured

tandem devices were fabricated in accordance to architecture shown in Fig. 1a, with MS-ITO as TRJ, and GuaBF$_4$ additive in WBG perovskite, and reached the best PCE of 25.6% with a V_{oc} of 2.034 V, a J_{sc} of 16.1 mA cm^{-2}, and FF of 78.2% (Supplementary Fig. 19). For substrate-configured tandems, we used a scraper to remove the edges of NBG back subcell before the deposition of the TRJ and WBG. The edge of the NBG subcell can be "self-encapsulated" by the device itself, which further improves the device stability (Fig. 4a inset). We placed 7 devices for each configuration without encapsulation in a glovebox filled with dry air (relative humidity, RH, below 20%). Unencapsulated superstrate-configured devices showed improved performance in the first 5 hours[2,61,62], but followed by a severe degradation in the next 40 hours. In contrast, unencapsulated substrate-configured tandem devices remained stable after being exposure to dry air for more than 250 hours, when using a self-encapsulated process, this value is 1000 hours. Meanwhile, we tracked the EQE of tandem devices to understand the degradation reasons. We found that for superstrate-configured tandems the EQE of the WBG was stable but the EQE of the NBG subcell decreased dramatically (Fig. 4b). For the substrate-configured devices, both WBG and NBG subcells did not show noticeable degradation in EQE following exposure to air for more than 1000 hours (Fig. 4c). To investigate the oxidation of NBG perovskites in air, we then exposed superstrate and substrate-configured all-perovskite tandems to dry air for 20 hours and 200 hours, respectively. We carried out XPS characterization of the NBG perovskite layers after removing the top layers by sticky tape and p-dichlorobenzene (Fig. 4d). Two obvious peaks at 486.2 eV and 487.1 eV, corresponding to Sn^{2+} and Sn^{4+}, respectively, were observed for superstrate-configured devices after exposure to air for 20 hours. In contrast, no significant Sn^{4+} signal peak was detected for the substrate-configured tandems after being exposed to air even for 10× longer period (200 hours).

We also investigated the operating stability of unencapsulated tandems under simulated 1-sun illumination and maximum power point (MPP) operation in a glovebox filled with dry air (Fig. 4e). The PCEs of both superstrate- and substrate-configured tandems increased slightly in the first few hours. The substrate-configured tandems did not exhibit any noticeable degradation after more than 200 hours of continuous operation. However, the unencapsulated superstrate-configured tandems degraded dramatically within 20 hours of continuous operation. Furthermore, the encapsulated substrate-configured tandems retained 100% of their initial performance following 600 hours of continuous operation, while the encapsulated superstrate-configured tandems experienced severe degradation after 340 hours of operation. We then tested the damp-heat stability (85 °C and relative humidity of 85%) of tandem devices with two different structures. Supplementary Fig. 20 shows that substrate-configured tandem devices exhibited improved stability under temperature of 85 °C and RH of 85% conditions. The substrate-configured tandems also showed better stability under high moisture and light

Table. 2 | PV performance of champion substrate-configured all-perovskite tandems with different substrates measured under AM1.5 illumination

Substrate	Scan direction	V_{oc}(V)	J_{sc}(mA cm^{-2})	FF(%)	PCE(%)
Glass (rigid)	Reverse	2.049	15.6	78.7	25.3
	Forward	2.021	15.6	79.5	25.1
PEN/Cu (flexible)	Reverse	2.017	15.6	76.2	24.1
	Forward	2.012	15.5	76.1	23.8
Cu foil (flexible)	Reverse	1.957	14.1	73.4	20.3
	Forward	1.944	14.6	73.5	20.8

Fig. 4 | Stability of substrate- and superstrate-configurated all-perovskite tandem solar cells. a Dark shelf stability of unencapsulated tandem devices stored in a glovebox filled with dry air (RH < 20%). The inset shows the schematic diagram of the oxidation process of NBG perovskite in superstrate- and substrate-configurated tandems, and a cross-section SEM image of the edge of a substrate-configurated tandem. **b, c** EQE spectra of superstrate- and substrate-configurated tandem during the aging process. **d** The *Sn 3d₅/₂* XPS spectra of NBG perovskite layers in superstrate- and substrate-configurated tandems. The superstrate-configurated and substrate-configurated tandems were aged in dry air for 20 and 200 hours, respectively. **e** Operating stability of unencapsulated superstrate- and substrate-configurated tandems, and encapsulated superstrate- and substrate-configurated tandems. The encapsulated device retained 100% of its initial efficiency after 600 hours of operation. All tests were carried out under 1-sun illumination (100 mW cm^{-2}) and MPP tracking.

soaking conditions (see Supplementary Note 2 and Supplementary Note 3).

Flexible substrate-configured tandems on opaque substrates
Due to the change of incident light direction, the substrate configuration widens the choice of flexible substrates, allowing the use of opaque materials such as metal foils and metal-coated polymer foils. We first fabricated flexible tandem solar cells on Cu-coated PEN substrates (device structure shown in Fig. 5a). The champion flexible substrate-configurated tandem had a PCE of 24.1% under reverse scan. The integrated J_{sc} values of the WBG and NBG subcells from EQE spectra (Fig. 5c) are 15.6 and 15.4 mA cm^{-2}, respectively, consistent with the J_{sc} determined from the $J–V$ measurements. We further carried out bending durability tests for flexible tandems. The flexible devices retained over 88% of their initial performance following 10,000 bending cycles with a bending curvature radius of 15 mm (Fig. 5d). The

When the bending radius was 12 mm, 10 mm and 8 mm, 90%, 78%, and 62% of the initial performance can be retained after 1000 bending cycles, respectively (Supplementary Fig. 21). Thick perovskite absorbers, as required for effective light absorption, used in those flexible tandems could be the main reason for the reduced mechanical stability under smaller bending radius. Using thinner absorbers is expected to significantly improve the flexibility, and nanophotonic strategies can be implemented to compensate for the inherent optical loss caused by the reduction of perovskite thickness. Advanced light-trapping techniques[63–66] will help reduce the thickness of WBG and NBG (and thus improve flexibility) while maintaining or even improving the efficiency of flexible tandems.

Furthermore, we fabricated tandem cells on Cu foils (thickness 25 μm) as the substrate, achieving a PCE of 20.3% (Fig. 5e). The integrated J_{sc} values of the WBG and NBG subcells from EQE spectra (Fig. 5f) are 14.8 and 14.0 mA cm^{-2}, respectively. The perovskite films
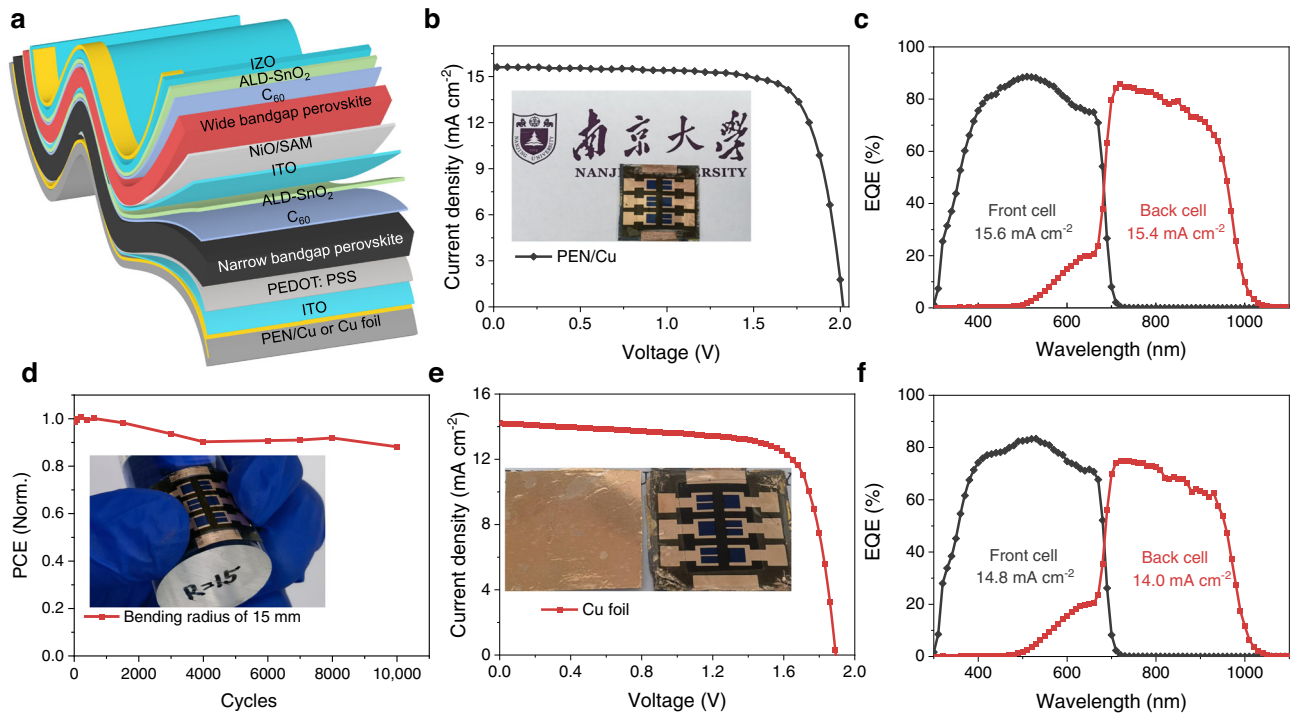
Fig. 5 | All-perovskite tandem solar cells on flexible opaque substrates. a Device structure of a flexible substrate-configured tandem. The substrate can be PEN or Cu-foils here. **b, c** $J–V$ curves, and EQE spectra of champion flexible substrate-configured tandems. The inset shows the image of a flexible substrate-configured tandem with an active area of 0.09 cm². **d** Bending tests of flexible substrate-configured tandem cells under a bending radius of 15 mm. The inset shows the digital image of a flexible substrate-configured tandem under bending. **e, f** $J–V$ curves, and EQE spectra of a Cu-foils flexible substrate-configured tandems. The inset shows the image of a flexible substrate-configured tandem using Cu-foils as substrate.

grown on different substrates (glass, PEN, and Cu foil) exhibited similar grain size and crystallinity (Supplementary Fig. 22). However, cracks were observed in the perovskite films deposited on Cu foil, which may be induced by stress release during perovskite crystallization. In addition, the much rougher surface on Cu foil, such as macroscopic cracks formed during the forging process, could be another reason for the worse performance observed in flexible tandems on Cu foil (Supplementary Fig. 23).

Discussion

In summary, we demonstrated the fabrication of all-perovskite tandems in substrate configuration on both rigid and flexible substrates. With the use of GuaBF₄ additives, we increased the V_{oc} and FF of semitransparent WBG PSCs. A PCE of 25.3% was obtained on all-perovskite tandem solar cells in substrate configuration. The substrate-configured devices exhibited exceptional resistance to oxidization and improved operational stability: the unencapsulated devices remained stable after being exposed to dry air for up to 1000 hours and the encapsulated devices retained 100% of their performance after 600 hours of operation at the MPP under full 1-sun illumination. Furthermore, we fabricated flexible tandem solar cells in substrate configuration with PCEs of 24.1% and 20.3% on PEN/Cu and Cu-foils, respectively. The advantages of substrate configuration in structure and stability provide new possibilities for commercial application of all-perovskite tandems. We found that the low J_{sc} due to the large reflection is another key factor limiting the performance of substrate-configured tandems. With proper optical optimization, PCE exceeding 30% will be anticipated[67–69].

Methods
Materials

All materials were used as received without further purification. The organic halide salts (FAI, FABr, MAI, FAI, GuaBF₄) were purchased from GreatCell Solar Materials (Australia). PEDOT:PSS aqueous solution (Al 4083) was purchased from Heraeus Clevios (Germany). 2PACz (>98.0%) and MeO-2PACz (>98.0%) were purchased from Tokyo Chemical Industry. PbI₂ (99.99%), PbBr₂ (99.99%)CsI (99.9%), and CsBr (99.9%) were purchased from TCI Chemicals. SnI₂ (99.999%) was purchased from Alfa Aesar. SnF₂ (99%), Indium tin oxide nanocrystals, DMF (99.8% anhydrous), DMSO (99.9% anhydrous), ethyl acetate (99.8% anhydrous), and chlorobenzene (99.8% anhydrous) were purchased from Sigma-Aldrich. C₆₀ was purchased from Nano-C (USA). BCP (>99% sublimed) was purchased from Xi'an Polymer Light Technology (China). Ftetrakis(dimethylamino) tin(iv) (99.9999%) was purchased from Ai Mou Yuan Scientific Equipment (Nanjing).

Perovskite precursor solution

Wide-bandgap $FA_{0.8}Cs_{0.2}Pb(I_{0.6}Br_{0.4})_3$ perovskite. The precursor solution (1.2 M) of wide-bandgap perovskite (-1.77 eV) was prepared in mixed solvents of DMF and DMSO with a volume ratio of 4:1. The molar ratio of FAI/FABr/CsI/CsBr/PbI₂/PbBr₂ was 0.48:0.32:0.12:0.08:0.6:0.4. GuaBF₄ was added to the precursor solution at optimized concentrations (1.5 mol% of Pb). The precursor solution was stirred at 50 °C for 2 hours and then filtered through 0.22-μm PTFE membrane prior to use.

Narrow-bandgap $FA_{0.7}MA_{0.3}Pb_{0.5}Sn_{0.5}I_3$ perovskite. The precursor solution was prepared in mixed solvents of DMF and DMSO with a volume ratio of 2:1. The molar ratios for FAI/MAI and PbI₂/SnI₂ were 0.7:0.3 and 0.5:0.5, respectively. The molar ratio of (FAI + MAI)/(PbI₂ + SnI₂) was 1:1. SnF₂ (10 mol% relative to SnI₂) was added to the precursor solution. The precursor solution was stirred at room temperature for 2 hours. Tin powders (5 mg mL⁻¹) and formamidine sulfinic acid (0.3 mol%) were added to the precursor to reduce Sn⁴⁺ in the precursor solution and to improve film uniformity. The precursor

solution was filtered through a 0.22-µm PTFE membrane before making perovskite films.

Device fabrication

Semitransparent single-junction wide-bandgap solar cells. The pre-patterned indium tin oxide glass substrates were sequentially cleaned using acetone and isopropanol. NiO was deposited by magnetron sputtering on ITO substrates first. Subsequently, the solutions of self-assembled molecule (SAM, 2PACz:MeO-2PACz = 3:1, 1 mmol mL^{-1} in IPA) were spin-coated on the NiO film at 4000 r.p.m. for 20 s, followed by annealing at 100 °C for 1 min in air. After cooling, we transferred the substrates immediately to a nitrogen-filled glovebox for the deposition of perovskite films. The perovskite films were deposited with two-step spin-coating procedures: (1) 2000 r.p.m. for 10 s with an acceleration of 200 r.p.m. s^{-1}. (2) 6000 r.p.m. for 40 s with an acceleration of 2000 r.p.m. s^{-1}. Chlorobenzene (200 µl) was dropped on the spinning substrate during the second spin-coating step at 20 s before the end of the procedure, followed by annealing at 100 °C for 5 min and 85 °C for 15 min. After cooling down to room temperature, the substrates were transferred to the evaporation system and 12 nm-C$_{60}$ was deposited at the rates of 0.2 Å s^{-1}. The substrates were transferred to the ALD system (Veeco Savannah S200) to deposit 15 nm SnO$_2$ at a low temperature of 75 °C. The 60 nm-IZO was deposited at room temperature with a background pressure of 4×10^{-4} Pa, working pressure of 0.5 Pa, Argon gas flow of 20 sccm and sputter power of 50 W. A 3-inch IZO target (90wt.% In$_2$O$_3$ and 10%wt. ZnO) was used for sputtering. Finally, 200 nm Cu was deposited by thermal evaporation as the front grid electrode. Usually, an anti-reflective film was used to reduce light reflection from the surface

Substrate configuration all-perovskite tandem solar cells. For rigid devices, the substrate is cleaned glass, while flexible devices are PEN or Cu foil fixed to the glass. 80 nm copper and 10 nm ITO were first deposited on the substrate (glass or PEN) by thermal evaporation and magnetron sputtering, respectively. In particular, for Cu foil tandem solar cells, only 10 nm ITO was needed to be deposited on the Cu surface. PEDOT: PSS was spin-coated on substrates at 4000 rpm for 30 s and annealed on a hotplate at 150 °C for 10 min in ambient air. After cooling, we transferred the substrates immediately to a nitrogen-filled glovebox for the deposition of perovskite films. The perovskite films were deposited with two-step spin-coating procedures: (1) 1000 rpm for 10 s with an acceleration of 200 rpm/s and (2) 4000 rpm for 40 s with a ramp-up of 1000 rpm/s. Ethyl acetate (300 µL) was dropped on the spinning substrate during the second spin-coating step at 20 s before the end of the procedure. The substrates were then transferred on a hotplate and heated at 100 °C for 10 min. After cooling down to room temperature, the substrates were transferred to the evaporation system and 20 nm-C$_{60}$ was deposited at the rates of 0.2 Å s^{-1}. In addition to the process described above, we used a scraper to remove the edges of NBG back subcell and then deposited the TRJ and WBG on it. The substrates were transferred to the ALD system to deposit 30 nm SnO$_2$ at a low temperature of 75 °C. The 15 nm-ITO was deposited at room temperature with a background pressure of 4×10^{-4} Pa, working pressure of 0.5 Pa, Argon gas flow of 20 sccm, and sputter power of 50 W. A 3-inch ITO target (90wt.% In$_2$O$_3$ and 10%wt. SnO$_2$) was used for sputtering. Subsequent processes are consistent with semitransparent wide-bandgap solar cells.

Characterization of solar cells

For semitransparent single-junction solar cells, the current density-voltage (J–V) characteristics were measured using a Keithley 2400 source meter under the illumination of the solar simulator (EnliTech, Class AAA) at the light intensity of 100 mW cm^{-2} as checked with NREL calibrated reference solar cells (KG-5 and KG-0 reference cells were used for the measurements of wide-bandgap and narrow-

bandgap solar cells, respectively). Unless otherwise stated, the J–V curves were all measured in air with a scanning rate of 100 mV s^{-1} (voltage steps of 20 mV and a delay time of 100 ms). The active area was determined by the aperture shade masks (0.0529 cm^2) placed in IZO side of the solar cells. EQE measurements were performed in ambient air using a QE system (EnliTech) with monochromatic light focused on device pixel and a chopper frequency of 20 Hz. For tandem solar cells, the J–V characteristics were carried out under the illumination of a two-lamp high spectral match solar simulator (SAN-EI ELECTRIC, XHS-50S1). EQE measurements were performed in ambient air, and the bias illumination from highly-bright LEDs with emission peaks of 850 and 460 nm were used for the measurements of the front and back subcells, respectively. No bias voltage was applied during the EQE measurements of tandems.

Stability tests of solar cells

The operational stability tests were carried out under full AM1.5 G illumination (Class AAA, multi-color LED solar simulator, Guangzhou Crysco Equipment Co. Ltd) with an intensity of 100 mW cm^{-2} using a home-build LabVIEW-based MPP tracking system and a *Perturb and observe* method. Unencapsulated samples were tested in a glovebox filled with dry air at a relative humidity of 10–18% and a temperature of 20–25 °C. Encapsulated samples were tested in an ambient air condition with a relative humidity of about 30–50% and a temperature of 20–25 °C. The solar cells were encapsulated with a cover glass and UV epoxy (Three Bond, Japan) which was cured under a UV-LED lamp (peak emission at 365 nm) for 3 min. No UV filter was applied during operation. The dark long-term shelf stability assessments of encapsulated devices were carried out by repeating the J-V characterizations over various times and the devices were stored in dry air too.

First-principles calculations

Electronic structure calculations were carried out within the framework of density functional theory using plane-wave pseudopotential method as implemented in the Vienna Ab initio Simulation Package. The electron-ion interactions were described by using the projected augmented wave pseudopotentials. The $6s^26p^2$ (Pb), $5s^25p^5$ (I), $2s^22p^2$ (C), $2s^22p^3$ (N), $3s^23p^3$ (P), $2s^22p^5$ (F), $2s^22p^1$ (B) were treated explicitly as valence electrons. We used the generalized gradient approximation formulated by Perdew, Burke, and Ernzerhof as exchange correlation functional. To simulate the FA$_{0.8}$Cs$_{0.2}$Pb(I$_{0.6}$Br$_{0.4}$)$_3$ perovskite surfaces and crystal boundary, we constructed FAPbI$_3$ perovskite $2 \times 2 \times 4$ supercells in the slab structures with a vacuum layer thickness of 15 Å. Structure optimization (including lattice parameters and internal atomic positions) was performed using the conjugate gradient technique until the energies converged to 10^{-4} eV. A kinetic energy cutoff of 400 eV was used for wave-function expansion and only the Γ point was used for Brillouin zone integration. To properly take into account the long-range van der Waals (vdW) interaction that is non-negligible for hybrid perovskites involving organic molecules, the vdW-optB86b functional was adopted.

Other characterizations

SEM images were obtained using a TESCAN microscope with an accelerating voltage of 2 kV. XRD patterns were collected using a Bruker D8 Advance equipped with a NaI scintillation counter and using monochromatized Copper Kα radiation (λ = 1.5406 Å). XPS analysis was carried out using the Thermo Scientific Al K-Alpha XPS system with energy steps of 0.1 eV. Steady-state PL and time-resolved PL were measured using an Edinburgh FLS980 system. The light was illuminated from the top surface of the perovskite film. For steady-state PL measurements, the excitation source was from a mono-chromated Xe lamp (peak wavelength at 520 nm with a line width of 2 nm). For time-resolved PL, a laser diode (λ = 405 nm) was used for the excitation source with an excitation power density of 0.06 nJ cm^{-2}. The PL decay

curves were fitted with biexponential function to obtain the fast and slow PL decay lifetimes of τ_1 and τ_2 and the corresponding coefficients of A_1 and A_2 of perovskite films, respectively. Then the PL effective decay lifetime τ_{eff} was calculated by the following equation: $\tau_{eff} = (A_1\tau_1 + A_2\tau_2)/(A_1 + A_2)$. Transient photovoltage decays were measured on a homemade system. A 540 nm green light-emitting diode was used to modulate the V_{oc} with a constant light bias, and the repetition rate was set to 2000 Hz. The open-circuit voltage transient, induced by the light perturbation, was measured with a digital oscilloscope set to an input impedance of 1 MΩ. The charge recombination lifetime was fitted by a single exponential decay.

Reporting summary

Further information on research design is available in the Nature Portfolio Reporting Summary linked to this article.

Data availability

The main data supporting the findings of this study are available within the published article and its Supplementary Information and source data files. Supplementary Figs. 2, 5, 6, 12, 16 are provided in the Supplementary Data 1–6 file. Additional data are available from the corresponding author on request. Source data are provided with this paper.

References

1. Tong, J. et al. Carrier lifetimes of 1 μs in Sn-Pb perovskites enable efficient all-perovskite tandem solar cells. *Science.* **364**, 475–479 (2019).
2. Lin, R. et al. Monolithic all-perovskite tandem solar cells with 24.8% efficiency exploiting comproportionation to suppress Sn(II) oxidation in precursor ink. *Nat. Energy* **4**, 864–873 (2019).
3. Eperon, G. E. et al. Perovskite-perovskite tandem photovoltaics with optimized band gaps. *Science.* **354**, 861–865 (2016).
4. Green, M. A. et al. Solar cell efficiency tables (Version 58). *Prog. Photovoltaics Res. Appl.* **29**, 657–667 (2021).
5. Lin, R. et al. All-perovskite tandem solar cells with improved grain surface passivation. *Nature* **603**, 73–78 (2022).
6. Li, Z. et al. Cost analysis of perovskite tandem photovoltaics. *Joule* **2**, 1559–1572 (2018).
7. Leijtens, T., Bush, K. A., Prasanna, R. & McGehee, M. D. Opportunities and challenges for tandem solar cells using metal halide perovskite semiconductors. *Nat. Energy* **3**, 828–838 (2018).
8. Boyd, C. C., Cheacharoen, R., Leijtens, T. & McGehee, M. D. Understanding degradation mechanisms and improving stability of perovskite photovoltaics. *Chem. Rev.* **119**, 3418–3451 (2019).
9. Song, Z. et al. A technoeconomic analysis of perovskite solar module manufacturing with low-cost materials and techniques. *Energy Environ. Sci.* **10**, 1297–1305 (2017).
10. Zhao, D. et al. Efficient two-terminal all-perovskite tandem solar cells enabled by high-quality low-bandgap absorber layers. *Nat. Energy* **3**, 1093–1100 (2018).
11. Yang, Z. et al. Enhancing electron diffusion length in narrow-bandgap perovskites for efficient monolithic perovskite tandem solar cells. *Nat. Commun.* **10**, 4498 (2019).
12. Palmstrom, A. F. et al. Enabling flexible all-perovskite tandem solar cells. *Joule* **3**, 2193–2204 (2019).
13. Werner, J. et al. Learning from existing photovoltaic technologies to identify alternative perovskite module designs. *Energy Environ. Sci.* **13**, 3393–3403 (2020).
14. Markvart, T. & McEvoy, A. Practical handbook of photovoltaics: fundamentals and applications. (Elsevier, 2003).
15. Fu, F. et al. High-efficiency inverted semi-transparent planar perovskite solar cells in substrate configuration. *Nat. Energy* **2**, 16190 (2017).
16. Wang, R. et al. A review of perovskites solar cell stability. *Adv. Funct. Mater.* **29**, 1808843 (2019).
17. Raga, S. R. et al. Influence of air annealing on high efficiency planar structure perovskite solar cells. *Chem. Mater.* **27**, 1597–1603 (2015).
18. Chung, I. et al. CsSnI$_3$: semiconductor or metal? High electrical conductivity and strong near-infrared photoluminescence from a single material. High hole mobility and phase-transitions. *J. Am. Chem. Soc.* **134**, 8579–8587 (2012).
19. Ke, W. & Kanatzidis, M. G. Prospects for low-toxicity lead-free perovskite solar cells. *Nat. Commun.* **10**, 965 (2019).
20. Chen, Q. et al. Unveiling roles of tin fluoride additives in high-efficiency low-bandgap mixed tin-lead perovskite solar cells. *Adv. Energy Mater.* **11**, 2101045 (2021).
21. Cao, J. et al. High-performance tin–lead mixed-perovskite solar cells with vertical compositional gradient. *Adv. Mater.* **34**, 2107729 (2021).
22. Lee, S. J. et al. Fabrication of efficient formamidinium tin iodide perovskite solar cells through SnF$_2$-pyrazine complex. *J. Am. Chem. Soc.* **138**, 3974–3977 (2016).
23. Tai, Q. et al. Antioxidant grain passivation for air-stable tin-based perovskite solar cells. *Angew. Chem. Int. Ed.* **58**, 806–810 (2019).
24. Xiao, K. et al. All-perovskite tandem solar cells with 24.2% certified efficiency and area over 1 cm^2 using surface-anchoring zwitterionic antioxidant. *Nat. Energy* **5**, 870–880 (2020).
25. Gao, H. et al. Thermally stable all-perovskite tandem solar cells fully using metal oxide charge transport layers and tunnel junction. *Sol. RRL* **2100814**, 2100814 (2021).
26. Kaltenbrunner, M. et al. Flexible high power-per-weight perovskite solar cells with chromium oxide-metal contacts for improved stability in air. *Nat. Mater.* **14**, 1032–1039 (2015).
27. Huang, K. et al. High-performance flexible perovskite solar cells via precise control of electron transport layer. *Adv. Energy Mater.* **9**, 1901419 (2019).
28. Chirilă, A. et al. Highly efficient Cu(In,Ga)Se$_2$ solar cells grown on flexible polymer films. *Nat. Mater.* **10**, 857–861 (2011).
29. Pianezzi, F. et al. Electronic properties of Cu(In, Ga)Se$_2$ solar cells on stainless steel foils without diffusion barrier. *Prog. Photovoltaics Res. Appl.* **20**, 253–259 (2012).
30. Kranz, L. et al. Doping of polycrystalline CdTe for high-efficiency solar cells on flexible metal foil. *Nat. Commun.* **4**, 2306 (2013).
31. Leijtens, T. et al. Tin-lead halide perovskites with improved thermal and air stability for efficient all-perovskite tandem solar cells. *Sustain. Energy Fuels* **2**, 2450–2459 (2018).
32. Wang, Y. et al. Recent progress in developing efficient monolithic all-perovskite tandem solar cells. *J. Semicond.* **41**, 051201 (2020).
33. Leijtens, T., Prasanna, R., Gold-Parker, A., Toney, M. F. & McGehee, M. D. Mechanism of tin oxidation and stabilization by lead substitution in tin halide perovskites. *ACS Energy Lett.* **2**, 2159–2165 (2017).
34. Lang, F. et al. Influence of radiation on the properties and the stability of hybrid perovskites. *Adv. Mater.* **30**, 1702905 (2018).
35. Conings, B. et al. Intrinsic thermal instability of methylammonium lead trihalide perovskite. *Adv. Energy Mater.* **5**, 1500477 (2015).
36. Wu, P. et al. Efficient and thermally stable all-perovskite tandem solar cells using All-FA narrow-bandgap perovskite and metal-oxide-based tunnel junction. *Adv. Energy Mater.* **12**, 2202948 (2022).
37. Prasanna, R. et al. Design of low bandgap tin–lead halide perovskite solar cells to achieve thermal, atmospheric and operational stability. *Nat. Energy* **4**, 939–947 (2019).
38. Tong, J. et al. High-performance methylammonium-free ideal-band-gap perovskite solar cells. *Matter* **4**, 1365–1376 (2021).
39. Jung, J. W., Williams, S. T. & Jen, A. K.-Y. Low-temperature processed high-performance flexible perovskite solar cells via rationally optimized solvent washing treatments. *RSC Adv.* **4**, 62971–62977 (2014).
40. Li, Z. et al. Wide-bandgap perovskite/gallium arsenide tandem solar cells. *Adv. Energy Mater.* **10**, 1903085 (2020).

41. Zheng, Y. C. et al. Thermal-induced volmer-weber growth behavior for planar heterojunction perovskites solar cells. *Chem. Mater.* **27**, 5116–5121 (2015).

42. Boccard, M. & Ballif, C. Influence of the subcell properties on the fill factor of two-terminal perovskite-silicon tandem solar cells. *ACS Energy Lett.* **5**, 1077–1082 (2020).

43. Li, L. et al. Flexible all-perovskite tandem solar cells approaching 25% efficiency with molecule-bridged hole-selective contact. *Nat. Energy* **7**, 2058–7546 (2022).

44. Mahesh, S. et al. Revealing the origin of voltage loss in mixed-halide perovskite solar cells. *Energy Environ. Sci.* **13**, 258–267 (2020).

45. Jodlowski, A. D. et al. Large guanidinium cation mixed with methylammonium in lead iodide perovskites for 19% efficient solar cells. *Nat. Energy* **2**, 972–979 (2017).

46. Kim, H., Lim, J., Sohail, M. & Nazeeruddin, M. K. Superhalogen passivation for efficient and stable perovskite solar cells. *Sol. RRL* **6**, 2200013 (2022).

47. Kim, D. et al. Efficient, stable silicon tandem cells enabled by anion-engineered wide-bandgap perovskites. *Science.* **368**, 155–160 (2020).

48. Zhang, J., Wu, S., Liu, T., Zhu, Z. & Jen, A. K. Y. Boosting photovoltaic performance for lead halide perovskites solar cells with BF_4 – anion substitutions. *Adv. Funct. Mater.* **29**, 1808833 (2019).

49. Wu, B. et al. Synergistic effect of guanidinium tetrafluoroborate boosting photovoltaic performance of perovskite solar cells. *Appl. Surf. Sci.* **603**, 154362 (2022).

50. Barkhouse, D. A. R., Gunawan, O., Gokmen, T., Todorov, T. K. & Mitzi, D. B. Yield predictions for photovoltaic power plants:empirical validation,recent advances and remaining uncertainties. *Prog. Photovoltaics Res. Appl.* **20**, 6–11 (2015).

51. Yang, L. et al. Zwitterionic ionic liquid confer defect tolerance, high conductivity, and hydrophobicity toward efficient perovskite solar cells exceeding 22% efficiency. *Sol. RRL* **5**, 2100352 (2021).

52. Nagane, S. & Ogale, S. $CH_3NH_3Pb(BF_4)_3$ and $(C_4H_9NH_3)_2Pb(BF_4)_4$ family of 3D and 2D perovskites without and with iodide and bromide ions substitution. *J. Phys. Chem. Lett.* **7**, 4757–4762 (2016).

53. Yu, Y. et al. Potassium tetrafluoroborate-induced defect tolerance enables efficient wide-bandgap perovskite solar cells. *J. Colloid Interface Sci.* **605**, 710–717 (2022).

54. Bush, K. A. et al. Thermal and environmental stability of semi-transparent perovskite solar cells for tandems enabled by a solution-processed nanoparticle buffer layer and sputtered ITO electrode. *Adv. Mater.* **28**, 3937–3943 (2016).

55. Huang, Y. et al. Stable layered 2D perovskite solar cells with an efficiency of over 19% via multifunctional interfacial engineering. *J. Am. Chem. Soc.* **143**, 3911–3917 (2021).

56. Nagane, S., Bansode, U., Game, O., Chhatre, S. & Ogale, S. $CH_3NH_3PbI_{(3−x)}(BF_4)_x$: molecular ion substituted hybrid perovskite. *Chem. Commun.* **50**, 9741 (2014).

57. Ma, K. et al. Multifunctional conjugated ligand engineering for stable and efficient perovskite solar cells. *Adv. Mater.* **33**, 2100791 (2021).

58. Huang, J., Yuan, Y., Shao, Y. & Yan, Y. Understanding the physical properties of hybrid perovskites for photovoltaic applications. *Nat. Rev. Mater.* **2**, 17042 (2017).

59. Pockett, A. & Carnie, M. J. Ionic influences on recombination in perovskite solar cells. *ACS Energy Lett.* **2**, 1683–1689 (2017).

60. Wolff, C. M. et al. Orders of recombination in complete perovskite solar cells – linking time-resolved and steady-state measurements. *Adv. Energy Mater.* **11**, 2101823 (2021).

61. Liu, Z. et al. Open-circuit voltages exceeding 1.26 V in planar methylammonium lead iodide perovskite solar cells. *ACS Energy Lett.* **4**, 110–117 (2019).

62. Rolston, N. et al. Light-induced lattice expansion leads to high-efficiency perovskite solar cells. *Science.* **368**, 67–70 (2020).

63. Haque, S. et al. Photonic-structured TiO_2 for high-efficiency, flexible and stable Perovskite solar cells. *Nano Energy* **59**, 91–101 (2019).

64. Haque, S. et al. Design of wave-optical structured substrates for ultra-thin perovskite solar cells. *Appl. Mater. Today* **20**, 100720 (2020).

65. Li, K. et al. Light trapping in solar cells: simple design rules to maximize absorption. *Optica* **7**, 1377 (2020).

66. Haque, S. et al. Photonic-structured perovskite solar cells: detailed optoelectronic analysis. *ACS Photonics* **9**, 2408–2421 (2022).

67. Shahiduzzaman, M. et al. Spray pyrolyzed TiO_2 embedded multi-layer front contact design for high-efficiency perovskite solar cells. *Nano-Micro Lett.* **13**, 1–17 (2021).

68. Hossain, M. I. et al. Perovskite/perovskite planar tandem solar cells: a comprehensive guideline for reaching energy conversion efficiency beyond 30%. *Nano Energy* **79**, 105400 (2021).

69. Akhtaruzzaman, M. et al. Nanophotonic-structured front contact for high-performance perovskite solar cells. *Sci. China Mater.* **65**, 1727–1740 (2022).

Acknowledgements

Author contributions

H.T. conceived and directed the overall project. Y.W., R.L., C.L., and Z.H. fabricated all the devices and conducted the characterization. X.W. and L.Z. carried out DFT calculations. M.Z., Ha.L., P.W., H.G., X.Z., M.L., M.I.S. L.L., Z.Z., Z.L., K.L., and R.L. helped with the device fabrication and material characterization. Y.W., Ho.L., Y.A., W.K., M.I.S., Y.G., and H.T. wrote the manuscript. All authors read and commented on the manuscript.

Competing interests

Additional information